IEEE Access
Multidisciplinary | Rapid Review | Open Access Journal

Received May 17, 2020, accepted June 20, 2020, date of publication July 1, 2020, date of current version July 14, 2020.

Digital Object Identifier 10.1109/ACCESS.2020.3006439

Performance Evaluation and Reliability of Flexible Asynchronous AC Link and LCC–HVDC Link Under Fault Conditions

IMDADULLAH[1,3], (Member, IEEE), ABDUL R. BEIG[2], (Senior Member, IEEE), AND M. SYED JAMIL ASGHAR[3], (Member, IEEE)

[1]Electrical Engineering Section, University Polytechnic, Aligarh Muslim University, Aligarh 202002, India
[2]Advanced Power and Energy Center, Department of Electrical Engineering and Computer Science, Khalifa University, Abu Dhabi 2533, United Arab Emirates
[3]Department of Electrical Engineering, ZHCET, Aligarh Muslim University, Aligarh 202002, India

Corresponding author: Imdadullah (imdadamu@gmail.com)

ABSTRACT Normally, HVDC links are used for the asynchronous interconnection of power system networks. Similarly, asynchronous AC links are also used for the same application. Here, the performance of a proposed flexible asynchronous AC link (FASAL) and a back-to-back line-commutated converter-based high-voltage direct current (BTB LCC-HVDC) link is evaluated and compared. These links are used for grid interconnection and to control the power transfer between interconnected grids. PSCAD/EMTDC based simulation model is developed for both the links. Modified CIGRE benchmark system is used for the simulation of the BTB LCC-HVDC link. The steady-state and dynamic simulations are carried out for the systems under consideration. The simulation results show that both the links are able to control power flow between the interconnected grids. It is evident from the results that the effect of fault is severe in the LCC-HVDC link as compared to FASAL system. Also, the impact of the fault on the healthy side grid is minimal in the FASAL as compared to the HVDC link.

INDEX TERMS Grid Interconnection, AC link, FASAL system, LCC-HVDC link, PSCAD/EMTDC Simulation, power flow controller.

NOMENCLATURE

ACA	Ant Colony algorithm.
CNT	Controllable network transformer.
DE	Differential Evolution.
DFIM	Doubly fed induction machine.
FACTS	Flexible AC transmission system.
FASAL	Flexible asynchronous AC link.
GA	Genetic Algorithm.
HSA	Harmony search algorithm.
IA	Immune Algorithm.
PSO	Particle Swarm Optimization.
RPFC	Rotary power flow controller.
SA	Simulated Annealing.
ST	Sen transformer.
STATCOM	Static synchronous compensator.
TCR	Thyristor controlled reactor.
TCPR	Thyristor-controlled phase-angle regulator.
TSC	Thyristor switched capacitor
VFT	Variable frequency transformer.

The associate editor coordinating the review of this manuscript and approving it for publication was Tariq Masood.

V_S, V_R	Sending, receiving end voltages.
X_L	Transmission line reactance.
δ	Phase angle.
$\boldsymbol{V_s}, \boldsymbol{V_r}$	Stator, rotor voltage vectors.
$\boldsymbol{I_s}, \boldsymbol{I_r}$	Stator, rotor current vectors.
$\boldsymbol{\psi_s}, \boldsymbol{\psi_r}$	Stator, rotor flux linkage vectors.
ω_s, ω_r	Stator, rotor angular frequency.
R_s, R_r	Stator, rotor resistance.
L_s, L_r	Stator, rotor self-inductance.
L_m	Mutual inductance.
$L_{\sigma s}, L_{\sigma r}$	Stator, rotor leakage inductance.
P_s, Q_s	Stator active and reactive power.
V_{dr}, V_{di}	Rectifier, inverter terminal voltage.
α_r, α_i	Ignition, extinction angle of rectifier and inverter.
a_r, a_i	Transformer taps setting at rectifier and inverter.
X_{cr}, X_{ci}	Commutation reactances in the rectifier and inverter.
I_d	Direct current.
μ	Overlap angle.

I. INTRODUCTION

Electric power grids are interconnected with the neighbouring grids for economic and reliable power supply. The power flow control between the interconnected grids in the desired path is necessary. The electric power industry is continuously searching for the most economical mode of bulk power transmission through a desired path. The overloading of the existing transmission lines is restricted by its thermal limit [1]. Electric power transfer through a transmission line is mainly rely upon the line reactance (X_L), magnitude of the voltages of both the sending and the receiving ends (V_S and V_R), and the phase angle (δ) between these voltages. The parameters which control the power transmission (voltage magnitude, reactance and phase angle) can be regulated by the use of the existing techniques, such as: (i) shunt inductor/capacitor for the control of voltage, (ii) phase-shifting transformers for the control of phase angle, (iii) series inductor/capacitor for the control of series reactance [2]–[4]. Nowadays, the parameters which control the amount and direction of power transmission can be controlled by the use of a number of power flow controllers. Some of them are given below.

The power electronic devices based Flexible AC Transmission System (FACTS) technology are found to be an effective alternative for controlling power and enhancing the usable capacity of present transmission systems. The key FACTS controllers include, thyristor-controlled phase-angle regulator (TCPR), static synchronous series compensator (SSSC), static synchronous compensator (STATCOM), unified power flow controller (UPFC), thyristor switched capacitor (TSC) and many more [3], [4]. The FACTS devices can also be classified as shunt, series and combination of both shunt-series depending upon their connection in the networks. These devices controls the bus voltages, line impedances, and phase angles in the power system rapidly and flexibly. Hence, FACTS devices can facilitate the power flow control, enhance the power transmission capability, decrease the generation cost, and improve the security and stability of power systems [5]. The maximum benefits which can be achieved by the FACTS installation depend upon their suitable ratings at optimal locations [6]. The problem of optimal placement of FACTS devices can be solved by analytical, linear programming and heuristic based procedures [7]. The common heuristic techniques for the optimal location of FACTS devices in the power system are Genetic Algorithm (GA), Simulated Annealing (SA), Immune Algorithm (IA), Particle Swarm Optimization (PSO), Differential Evolution (DE), Harmony search algorithm (HSA), and Ant Colony algorithm (ACA) etc. [8]. However, the implementation of FACTS devices in the power system is restricted due to injection of harmonics into the electric power networks, high cost and complexity [9], [10].

The high voltage direct current (HVDC) is used to interconnect two electric power grids and to control the power transmission between them which may be synchronous or asynchronous. It uses two basic topologies namely, line-commutated converters (LCC) and voltage source converters (VSC) including both back–to–back (BTB) and point–to–point topologies [11]–[14]. The LCC technology is a mature technology which is suitable for low cost, long distance and bulk power transmission [15]. On the other hand VSC has advantages of enhanced efficiency of power transmission, reactive power compensation, multi-terminal (MT) topology, and independency and flexibility in power control. Hence, VSC-HVDC offers a feasible alternative for city centers in-feed, power supply to islands, grid interconnection and offshore wind farms (OWF) integration [16]. However, the design, coordinated controls, requirement of large filter banks and need of reactive power compensation makes the HVDC system complicated and costly [17].

There are other types of power flow controllers available which include, Sen transformers (ST) [18], [19], rotary power flow controllers (RPFC) [20], [21], controllable network transformers (CNT) [22], variable frequency transformers (VFT) [23]–[25].

The Sen transformer (ST) improve the regulation performance of the conventional phase-shifting transformer (PST). The ST uses a three-phase four-winding transformer along with a three sets of tap changers which injects a voltage of variable magnitude and phase angle. The ST independently control the active and reactive power flow through the transmission line [26]. However, operation is step-wise due to use of tap changers in ST [27].

The rotary power flow controllers (RPFC) is introduced for continuous control of power flow in an electric power transmission corridor. It can be achieved by the injection of a controlled amount of series voltage in the transmission line. The phase shift of the injected series voltage controls the real power flow and its magnitude controls the reactive flow in the transmission line. An RPFC consists of conventional series and shunt transformers, and two rotary phase-shifting transformer (RPST) [28]. However, the RPFC needs separate, high power and special drive systems for the rotation of the rotor shaft of two rotary phase-shifting transformer (RPST) [29].

The variable frequency transformer (VFT) is a power transmission technology which provide bidirectional power flow control between two power system networks. It consists of a wound rotor induction machine (WRIM) having three-phase windings on both stator and rotor. One power system network is connected to the stator windings and another power system network is connected to the rotor windings of the VFT. A dc motor and its drive system is employed to control the torque applied to the rotor shaft of the WRIM. In order to control the power transfer through the VFT, a closed-loop control is applied to regulate the rotor position with respect to the stator [30]. Moreover, a separate DC drive system is employed for regulating the speed, torque, and position of the rotor shaft. This indeed regulates the amount and direction of power transmission between the interconnected electric networks. However, the VFT system needs periodical shutdown and maintenance for the replacement of carbon brushes of the DC motor [31]. Moreover, under severe fault condition, very

high torque is required for the compensation of the fault [32]. Therefore, a high power DC motor and its drive system is necessary [33].

A recently developed and reported asynchronous AC link called flexible asynchronous AC link (FASAL) system is also capable of controlling the power flow between AC networks [34]. Therefore, it is desirable to evaluate and compare new techniques with the existing techniques. Since, LCC-HVDC is a well established and mature technology [35], therefore, focus of this paper is to evaluate and compare the performance of FASAL system with BTB LCC–HVDC system used for grid interconnection and power flow control. The main contributions of this paper are stated below.

- The steady-state mathematical model is developed and expressions for stator and rotor power is derived for the doubly-fed induction machines (DFIM) used as freely rotating transformer.
- The dynamic model of a DFIM is also presented and the equations describing the DFIM under dynamic conditions are summarized.
- The simulation model of FASAL system is developed using PSCAD/EMTDC software and its performance during steady-state condition is evaluated.
- The performance of the FASAL system under various fault conditions such as LG, LLG and LL is evaluated.
- The steady-state mathematical model of a LCC-HVDC is presented and the equations describing the two-terminal LCC-HVDC link are summarized.
- The simulation model of the conventional back-to-back line-commutated converter-based high-voltage direct current (BTB LCC-HVDC) system is developed which is based on modified CIGRE benchmark model using PSCAD/EMTDC software and its performance during steady-state condition is evaluated.
- The performance of the BTB LCC-HVDC system under various fault conditions such as LG, LLG and LL is evaluated using PSCAD/EMTDC software.
- A comparative analysis between FASAL system and BTB LCC-HVDC system is made under steady-state and various fault conditions.

The remaining part of this paper is organized as follows. In section II, system description and steady-state mathematical model of proposed FASAL system are presented. In section III, steady-state and dynamic simulation analysis of FASAL is described. In section IV, system description and steady-state mathematical model of LCC-HVDC link are presented. The steady-state and dynamic simulation analysis of LCC-HVDC link is presented in section V. In section VI, comparative analysis of FASAL system and BTB LCC-HVDC are reported. Finally, the paper is concluded in section VII.

II. DESCRIPTION OF FASAL SYSTEM

A FASAL system is an asynchronous power transmission link which is recently developed and reported [34]. It is a combination of doubly fed induction machine (DFIM), voltage regulator and frequency converters. A power source, Grid–1 (having voltage, V_1 and frequency, f_1) is connected to the stator of DFIM and another power source, Grid–2 (having voltage, V_2 and frequency, f_2) is connected to the rotor of DFIM. Three-phase symmetrical balanced windings with equal number of poles is placed on both the stator and the rotor. A universal configuration of the FASAL system linking two independent grid is presented in Fig. 1. The amount and direction of power transfer are controlled by regulating the voltage and frequency [36].

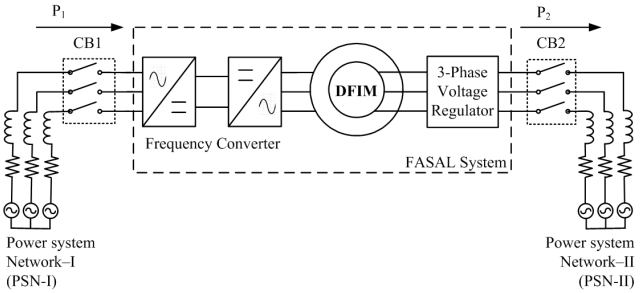

FIGURE 1. A general configuration of FASAL system linking two independent power system networks.

The active power is transmitted from the higher frequency network (grid) to the lower frequency network (grid). If Grid–1 and Grid–2 are operating at 60 Hz and 50 Hz, respectively, then, the active power flows from Grid–1 to Grid–2 without any use of the frequency converter. Then, the amount of power flow is controlled by regulating the voltage magnitude by the voltage regulator. When both grids are operating at the same frequency (e.g., 50 Hz), a frequency converter is employed to raise the frequency which in tern controls the power flow [37].

III. MATHEMATICAL MODEL

A. STEADY-STATE MODEL OF DFIM

A simplified single-phase equivalent circuit of a DFIM referred to the stator-side is considered to analyze the real and reactive power flow through the DFIM as shown in Fig. 2. The impedance of the DFIM when neglecting the magnetizing branch (as magnetizing impedance, Z_m is very high) is given by, $Z = R + jX$, where,

$$Z = R_1 + \frac{R_2}{s} + j(\omega_1 L_1 + \omega_1 L_2) \tag{1}$$

The simplified expressions of stator and rotor powers P_1 and P_2 are derived by using the steady-state equivalent circuit model (Fig. 2). The apparent power S_1 on the stator side is given by,

$$S_1 = P_1 + jQ_1 = (V_1 \angle 0) I_1^* \tag{2}$$

The expression of current I_1 and I_1^* are derived from equivalent circuit shown in Fig. 2 as,

$$I_1 = \frac{(V_1 - V_2/s\cos\delta - jV_2/s\sin\delta)}{R + jX} \tag{3}$$

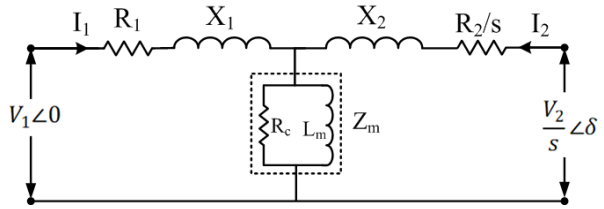

FIGURE 2. Single-phase steady-state equivalent circuit of the DFIM referred to stator side.

$$I_1^* = \left[\frac{R(V_1 - \frac{V_2}{s}\cos\delta) - X\frac{V_2}{s}\sin\delta}{R^2 + X^2}\right] + j\left[\frac{X(V_1 - \frac{V_2}{s}\cos\delta) + R\frac{V_2}{s}\sin\delta}{R^2 + X^2}\right] \quad (4)$$

where $R = (R_1 + R_2/s)$, and $X = (X_1 + X_2)$

From (2), the stator apparent power can be written as,

$$S_1 = \left[\frac{R(V_1 - \frac{V_2}{s}\cos\delta) - X\frac{V_2}{s}\sin\delta}{R^2 + X^2}\right] V_1 + j\left[\frac{X(V_1 - \frac{V_2}{s}\cos\delta) + R\frac{V_2}{s}\sin\delta}{R^2 + X^2}\right] V_1 \quad (5)$$

Thus, the real power (P_1) and reactive power (Q_1) at the stator side are:

$$P_1 = \left[X\frac{V_2}{s}\sin\delta - R(V_1 - \frac{V_2}{s}\cos\delta)\right]\left(-\frac{V_1}{Z^2}\right) \quad (6)$$

$$Q_1 = \left[R\frac{V_2}{s}\sin\delta + X(V_1 - \frac{V_2}{s}\cos\delta)\right]\left(\frac{V_1}{Z^2}\right) \quad (7)$$

where $Z = R + jX$

The apparent power S_2 on the rotor side is given by,

$$S_2 = P_2 + jQ_2 = \left(\frac{V_2\angle\delta}{s}\right) I_2^* \quad (8)$$

The expression of current I_2 and I_2^* based on equivalent circuit shown in Fig. 2, are given by

$$I_2 = \frac{(\frac{V_2}{s}\cos\delta + j\frac{V_2}{s}\sin\delta) - V_1}{R + jX} \quad (9)$$

$$I_2^* = \left[\frac{X\frac{V_2}{s}\sin\delta + R(\frac{V_2}{s}\cos\delta - V_1)}{R^2 + X^2}\right] - j\left[\frac{R\frac{V_2}{s}\sin\delta + X(V_1 - \frac{V_2}{s}\cos\delta)}{R^2 + X^2}\right] \quad (10)$$

From (8), the rotor apparent power S_2 is given by

$$S_2 = \left(\frac{V_2}{s}\cos\delta + j\frac{V_2}{s}\sin\delta\right) * I_2^* = \left[\frac{R\frac{V_2^2}{s^2} + V_1\frac{V_2}{s}(X\sin\delta - R\cos\delta)}{R^2 + X^2}\right] + j\left[\frac{X\frac{V_2^2}{s^2} - V_1\frac{V_2}{s}(X\cos\delta + R\sin\delta)}{R^2 + X^2}\right] \quad (11)$$

Therefore, the rotor real and reactive power at rotor side are:

$$P_2 = \left[R\frac{V_2}{s} + V_1(X\sin\delta - R\cos\delta)\right]\left(\frac{V_2}{sZ^2}\right) \quad (12)$$

$$Q_2 = \left[X\frac{V_2}{s} - V_1(X\cos\delta + R\sin\delta)\right]\left(\frac{V_2}{sZ^2}\right) \quad (13)$$

It is evident from the above expression that the power depends on the voltage and the frequency.

B. DYNAMIC MODEL OF DFIM

The equivalent circuit of a DFIM is represented in an arbitrary reference frame rotating at angular speed of ω is shown in Fig. 3 [38]. According to Fig. 3, the stator and rotor flux ψ_s and ψ_r are given as:

$$\psi_s = L_s.\boldsymbol{I_s} + L_m.\boldsymbol{I_r}$$
$$\psi_r = L_r.\boldsymbol{I_r} + L_m.\boldsymbol{I_s} \quad (14)$$

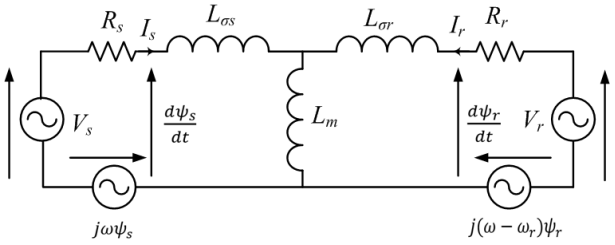

FIGURE 3. Equivalent circuit of a DFIM in rotating reference frame.

The stator and rotor voltages $\boldsymbol{V_s}$ and $\boldsymbol{V_r}$ in the arbitrary reference frame can be expressed as [39]:

$$\boldsymbol{V_s} = R_s.\boldsymbol{I_s} + \frac{d\psi_s}{dt} + j\omega.\psi_s \quad (15)$$

$$\boldsymbol{V_r} = R_r.\boldsymbol{I_r} + \frac{d\psi_r}{dt} + j(\omega - \omega_r).\psi_r \quad (16)$$

Using (14), the rotor flux and stator current can be expressed as:

$$\psi_r = \frac{L_m}{L_s}.\boldsymbol{\psi_s} + \sigma L_r\boldsymbol{I_r}$$
$$\boldsymbol{I_s} = \frac{1}{L_s}(\boldsymbol{\psi_s} - L_m\boldsymbol{I_r}) \quad (17)$$

where $\sigma = (L_sL_r - L_m^2)/(L_sL_r)$ is the leakage factor.

From (17) and (16), the rotor voltage in the arbitrary rotating reference frame is given by

$$\boldsymbol{V_r} = R_r.\boldsymbol{I_r} + \sigma L_r\frac{d\boldsymbol{I_r}}{dt} + \frac{L_m}{L_s}\frac{d\boldsymbol{\psi_s}}{dt} + j(\omega - \omega_r)\left(\sigma L_r.\boldsymbol{I_r} + \frac{L_m}{L_s}.\boldsymbol{\psi_s}\right) \quad (18)$$

Under balanced network conditions, the amplitude and rotating speed of the stator flux are constant. Therefore, the stator flux remains constant, i.e., $\frac{d\psi_s}{dt} = 0$. Neglecting the voltage drop across the stator resistance, the stator voltage in (15) can be simplified as [40]:

$$\boldsymbol{V_s} \approx j\omega.\psi_s \quad (19)$$

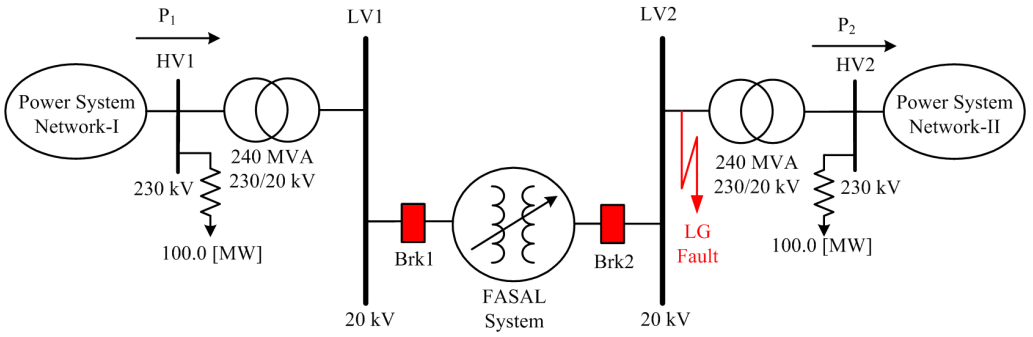

FIGURE 4. FASAL configuration used for steady-state and dynamic simulations.

When the d-axis of the reference frame is fixed to the stator flux rotating at the synchronous speed (ω_s). The expressions for $\boldsymbol{V_s}$ and $\boldsymbol{V_r}$ in the new reference frame can be derived by replacing ω with ω_s in (15), (16) and (18).

The stator apparent power can be expressed as:

$$S_s = P_s + jQ_s = -\frac{3}{2}\boldsymbol{V_s} \times \hat{\boldsymbol{I}}_{\boldsymbol{s}} \approx -\frac{3}{2}j\omega.\psi_s \times \frac{1}{L_s}(\hat{\boldsymbol{\psi}}_{\boldsymbol{s}} - L_m\boldsymbol{I_r}) \quad (20)$$

where $\hat{\boldsymbol{I}}_{\boldsymbol{s}}$ is the conjugated space vector of $\boldsymbol{I_s}$. Separating (20) into real and imaginary parts, the stator active and reactive power are:

$$P_s = \frac{3}{2}\frac{\omega_s}{L_s}\psi_s L_m I_{rq}$$
$$Q_s = -\frac{3}{2}\frac{\omega_s}{L_s}\psi_s(\psi_s - L_m I_{rd}) \quad (21)$$

IV. SIMULATION STUDIES OF FASAL SYSTEM

The FASAL system is simulated in PSCAD/EMTDC simulation environment. The parameters used for simulations are given in Appendix A and Appendix B [36]. Two grids (i.e., Grid–1 and Grid–2) are considered identical with different operating frequencies. The stator and the rotor of the FASAL system is connected to 240 MW, 230 kV, 60 Hz and 240 MW, 230 kV, 50 Hz grids through a 20/230 kV transformer. The rating of FASAL system is taken as 20 kV and 200 MW. The steady–state and the dynamic conditions are simulated to evaluate the behaviour of the FASAL system.

A. STEADY-STATE SIMULATIONS

The switching of circuit breaker, Brk–1 at $t = 0.5$ s, connect the stator terminals with Grid–1 (Power System Network-I) which is operating at 60 Hz. The rotor is connected to the Grid–2 (Power System Network-II) which is operating at 50 Hz by switching of Brk–2 at $t = 1.0$ s as shown in Fig. 4. Moreover, Brk-3 is considered closed during complete simulation period and fault does not applied under steady-state condition. The active power flows from higher frequency network to lower frequency network, therefore, active power flows from Grid-1 to Grid-2 [36]. The simulation results of stator voltage,rotor voltage, stator current, rotor current, real power and reactive power under steady-state condition are shown in Fig. 5. The power fed to the Grid–2 is about 186.00 MW and the real power available at Grid-1 is 227 MW at grid voltages, $V_1 = V_2 = 230$ kV and frequency, $f_1 = 60$ Hz, $f_2 = 50$ Hz (Fig. 5e). Moreover, under same condition the reactive power $Q_1 = 180$ MVAr and $Q_2 = 120$ MVAr as shown in Fig. 5f. The simulation results of power transmission with respect to voltage, V_2 while keeping voltage V_1 constant and frequency, $f_1 = 60$ Hz, $f_2 = 50$ Hz in given in Table 1.

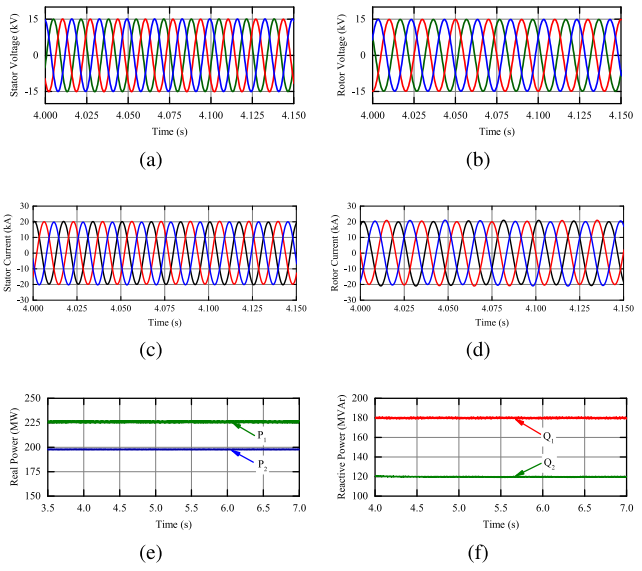

FIGURE 5. Simulation results of FASAL system under steady-state condition. (a) instantaneous (3-phase) stator voltage. (b) instantaneous (3-phase) rotor voltage. (c) instantaneous (3-phase) stator current. (d) instantaneous (3-phase) rotor current. (e) Real Power flow. (f) Reactive power.

B. DYNAMIC SIMULATIONS

The resiliency of the FASAL system under dynamic conditions is also evaluated using PSCAD/EMTDC based simulations. In this section, three types of faults are simulated, namely single-line-to-ground (LG) fault, double-line-to-ground (LLG) fault and line-to-line (LL) fault on the rotor side of the DFIM (receiving end side).

TABLE 1. Power transmission through the FASAL system with respect to the voltage V_2.

Voltage V_2 (kV)	Power P_1 (MW)	Power P_2 (MW)	η of power transmission (%)
10	126.66	93.59	73.89
11	147.89	109.69	74.17
12	167.63	126.14	75.25
13	183	140.53	76.79
14	190.65	153.92	80.73
15	205.58	165.06	80.29
16	212.58	173.27	81.51
17	219.75	179.65	81.75
18	225.6	184.67	81.86
19	226.44	185.69	82.00
20	227.05	186.72	82.24

1) SINGLE-LINE-TO-GROUND (LG) FAULT ON THE ROTOR SIDE

A single-line to ground (LG) fault is simulated in phase-A on the rotor side of the DFIM (Grid-2 side) as shown in Fig. 4. The fault is applied at $t = 4.0s$ and cleared at $t = 4.05s$, hence, the duration of fault is $0.05s$. Figs. 6a and 6b show the simulated results of instantaneous stator and rotor voltages during the LG fault on the rotor side. It is evident from these figures that there is transient in the rotor voltage from $t = 4.0s$ to $t = 4.05s$ whereas a little effect was observed on stator voltage during the fault period. The simulated instantaneous 3-phase stator and rotor currents during the LG fault on the rotor side is presented in Figs. 6c and 6d. It is evident from Figs. 6c and 6d that the effect of LG fault is small on both rotor and stator current. The simulation results of real power on the stator side (Grid–1) and the real power transmitted to the rotor side (Grid–2) during the LG fault condition is presented in Fig. 6e. It can be seen that there is dip of about 20 MW in real power transferred to the Grid–2 while about 12 MW dip in real power is observed on stator side (Grid–1) or healthy side during the LG fault on rotor side (Fig. 6e). The simulated results of reactive power under LG fault on rotor side is shown in Fig. 6f. This shows that the effect of fault is little on reactive power.

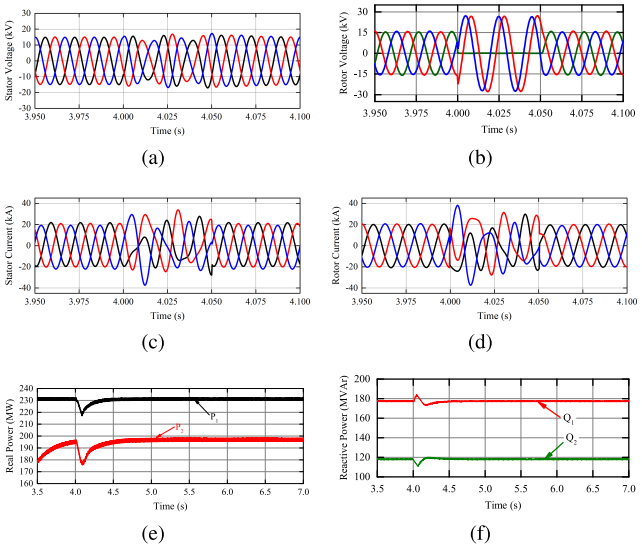

FIGURE 6. Simulation results of FASAL system under the LG fault on the Bus LV2 side. (a) instantaneous (3-phase) stator voltage. (b) instantaneous (3-phase) rotor voltage. (c) instantaneous (3-phase) stator current. (d) instantaneous (3-phase) rotor current. (e) Real power flow. (f) Reactive power.

Thus, the performance of the FASAL system during the single-phase-to-ground fault on rotor side is excellent as the healthy side remains almost unaffected. Thus, FASAL system is highly reliable.

2) DOUBLE-LINE-TO-GROUND (LLG) FAULT ON THE ROTOR SIDE

A double-line-to-ground (LLG) fault is simulated on the rotor side. The fault is applied at $t = 4.0s$ and cleared at $t = 4.05s$, hence, the duration of fault is $0.05s$.

The simulated instantaneous stator and rotor voltages during the LLG fault on rotor side are shown in Figs. 7a and 7b. There is sharp dip in the rotor voltage during the fault period and very small effect is observed on the stator voltage. The simulated results of instantaneous stator and rotor currents during the LLG fault on the rotor side are presented in Figs. 7c and 7d. The rotor current increases abruptly during the fault period, thereafter reaches to its normal value. It is also evident that, the LLG fault on rotor side has little effect on stator currents as the unbalance appears during the fault period only.

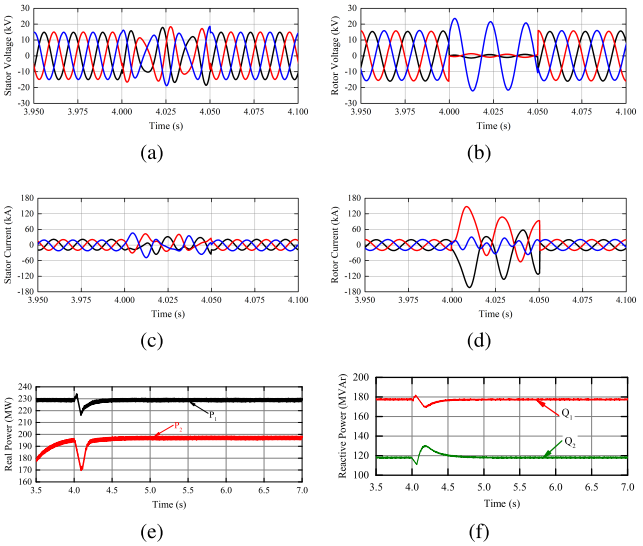

FIGURE 7. Simulation results of FASAL system under the LLG fault on the Bus LV2 side. (a) instantaneous (3-phase) stator voltage. (b) instantaneous (3-phase) rotor voltage. (c) instantaneous (3-phase) stator current. (d) instantaneous (3-phase) rotor current. (e) Real power flow. (f) Reactive power.

The simulated results of real power at the stator side (Grid-1) and the rotor side (Grid-2) during the LLG fault on

the rotor side is shown in Fig. 7e. It is evident that there is about 25 MW dip in the real power transferred to the rotor side (Grid-2) while comparatively small dip (about 15 MW) in the real power on the stator side (Grid-1) during the fault period. When fault is cleared the power transfer reaches to its normal value. The reactive power also exhibit fluctuations during LLG fault on rotor side (Fig. 7f).

Therefore, the performance of the FASAL system during the double-line-to-ground (LLG) fault is also satisfactory. The healthy side power system network remains practically unaffected.

3) LINE-TO-LINE (LL) FAULT ON THE ROTOR SIDE

A double–line (LL) fault is simulated on the rotor side. The fault is applied at $t = 4.0s$ and cleared at $t = 4.05s$, hence, the duration of fault is $0.05s$.

The simulated instantaneous stator and rotor voltages during the LLG fault on rotor side are shown in Figs. 8a and 8b. There is sharp dip in the rotor voltage during the fault period and very small effect is observed on the stator voltage as depicted in Fig. 8g. The simulated results of instantaneous stator and rotor currents during the LL fault on the rotor side are presented in Figs. 8c and 8d. The rotor current increases abruptly during the fault period, thereafter reaches to its normal value. It is also evident that, the LL fault on rotor side has effect on stator currents as the unbalance and overshoots appears during the fault period only. The simulated results of real power at the stator side (Grid-1) and the rotor side (Grid-2) during the LL fault on the rotor side is shown in Fig. 7e. It is evident that there is about 27 MW dip in the real power transferred to the rotor side (Grid-2) while comparatively small dip (about 15 MW) in the real power on the stator side (Grid-1) during the fault period. When fault is cleared the power transfer reaches to its normal value. The reactive power demand increases upto 40 MVAr during LL fault on rotor side (Fig. 7f).

Therefore, the performance of the FASAL system during the double-line (LL) fault is also satisfactory. The healthy side power system network remains practically least affected.

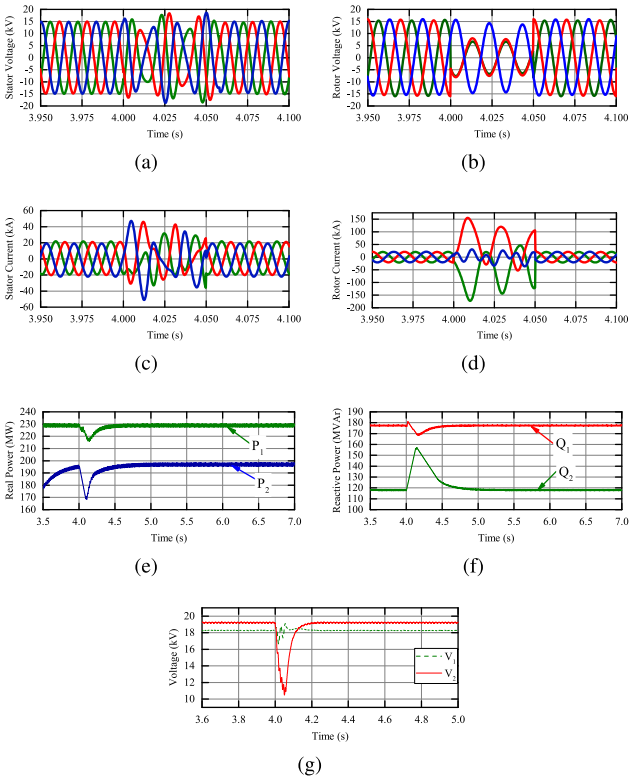

FIGURE 8. Simulation results of FASAL system under the LL fault on the Bus LV2 side. (a) instantaneous (3-phase) stator voltage. (b) instantaneous (3-phase) rotor voltage. (c) instantaneous (3-phase) stator current. (d) instantaneous (3-phase) rotor current. (e) Real power flow. (f) Reactive power.

V. DESCRIPTION AND MODELING OF BTB LCC-HVDC SYSTEM

Nowadays, an HVDC system become an important technology for long distance, bulk power transmission, grid interconnection and submarine cable power transmission. The conventional thyristor-based LCC-HVDC technology is still attractive due to reduced power losses, low capital cost, higher stability, and higher reliability for large-scale HVDC networks [35]. Therefore, the proposed system is compared with a well-established and commonly used LCC-HVDC technology.

A typical BTB LCC-HVDC link interconnecting two electric power grids (Grid-1 and Grid-2) is shown in Fig. 9. The CIGRE Benchmark model which provides reference for HVDC system studies is modified as BTB LCC-HVDC [41]. To assess the behavior of the system, the steady-state and dynamic conditions are simulated using PSCAD/EMTDC.

A. STEADY-STATE MODEL OF LCC-HVDC

The HVDC links can be represented by an equivalent HVDC model which consists of two converter stations and a DC transmission line. This equivalent model is irrespective of type of connection and the number of bridges. In the LCC-HVDC link, the converters perform AC/DC and DC/AC conversions which consist of valve bridges and load tap changer (LTC) transformers. The valve bridge is an array of thyristors that sequentially connect each phase of the ac three-phase system at the appropriate point of the voltage cycle to produce direct current. The most frequent configurations of HVDC link are monopole and bipolar. The monopole employed one conductor to deliver the power and either the ground or a metallic conductor as a return path. The bipolar topology employed two conductors one for positive and one for negative, and may require a return path. The steady-state analysis of LCC-HVDC system is carried out using the assumptions listed below [42].

- The AC source appeared at the converter terminals is balanced (three phase voltages and currents), a sinusoidal voltage waveform having constant amplitude and frequency.

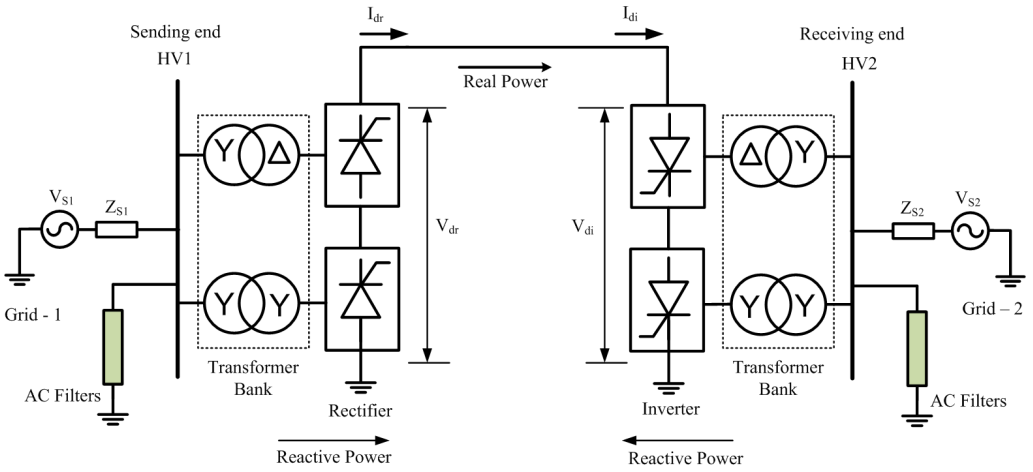

FIGURE 9. A typical BTB LCC-HVDC link interconnecting Grid-1 and Grid-2.

- All harmonic voltages and currents produced by the converter are filtered out and are not reach to the AC system.
- The converter transformers have no resistance and no magnetising reactance.
- The converter has no active power loss because the valves are considered ideal with no voltage drop.
- The DC voltage and current are free from ripple.

Based on the above assumptions, the magnitudes of DC voltage at rectifier terminal (V_{dr}) and at the inverter terminal (V_{dr}) are given as [43]:

$$V_{dr} = \frac{3\sqrt{2}}{\pi}(np_r)a_r V_r \cos\alpha_r - \frac{3}{\pi}X_{cr}(np_r)I_d \quad (22)$$

$$V_{di} = \frac{3\sqrt{2}}{\pi}(np_i)a_i V_i \cos\alpha_i - \frac{3}{\pi}X_{ci}(np_i)I_d \quad (23)$$

where np_r and np_i are the number of series-connected bridges in the rectifier and inverter, respectively; a_r and a_i are the transformer taps setting at rectifier and inverter, respectively; α_r and α_i are the ignition angle and extinction angle of rectifier and inverter, respectively; V_r and V_i are the effective voltage magnitude at the AC terminals of the rectifier and inverter, respectively; X_{cr} and X_{ci} are the commutation reactances in the rectifier and inverter, respectively. I_d is the direct current.

The real power flowing at the terminals of the rectifier and inverter is given by

$$P_{dr} = V_{dr}I_d \quad (24)$$

$$P_{di} = V_{di}I_d \quad (25)$$

The reactive power flowing into the AC terminals of the rectifier and the inverter is given by

$$Q_{dr} = P_{dr}\tan\varphi_r \quad (26)$$

$$Q_{di} = P_{di}\tan\varphi_i \quad (27)$$

where φ_r and φ_i are the angles by which the fundamental line current (ζ) lags with the source voltage (line to neutral). The δ is angle between both the source voltages.

The phase currents cannot change instantly during the commutation process.Therefore, the transfer of current from one phase to another requires a finite time which is called as commutation time or overlap time. This overlap or commutation angle is denoted by μ [1]. A short-circuit of short duration takes place between the two commuting thyristors during the overlap period leading to dc voltage reduction temporarily. This effect does not appear in the set of equations presented above. However, it is considered by means of the commutation resistance.

When considering an overlap angle μ less than 60 degree, the angles φ_r and φ_i can be expressed as below [42], [44]:

$$\tan\varphi_r = \frac{2\mu_r + \sin 2\alpha_r - \sin 2(\alpha_r + \mu_r)}{\cos 2\alpha_r - \cos 2(\alpha_r + \mu_r)} \quad (28)$$

$$\tan\varphi_i = \frac{2\mu_i + \sin 2\alpha_i - \sin 2(\alpha_i + \mu_i)}{\cos 2\alpha_i - \cos 2(\alpha_i + \mu_i)} \quad (29)$$

The overlap angle μ on both the rectifier and inverter sides may be given as follows:

$$\mu_r = \cos^{-1}\left(\cos\alpha_r - \frac{2r_{cr}I_d}{a_r V_r}\right) - \alpha_r \quad (30)$$

$$\mu_i = \cos^{-1}\left(\cos\alpha_i - \frac{2r_{ci}I_d}{a_i V_i}\right) - \alpha_i \quad (31)$$

Moreover, the direct current through the DC link can be expressed as:

$$I_d = \frac{V_{dr} - V_{di}}{R_C} \quad (32)$$

where R_C is the DC resistance of the cable.

VI. SIMULATION STUDIES OF BTB LCC-HVDC LINK

A. STEADY-STATE SIMULATIONS

The steady-state condition is simulated assuming that the real power flows from Grid-1 to Grid-2, where as Grid-1

is operating at 60 Hz and Grid-2 is operating at 50 Hz. The simulated results of rectifier side and inverter side AC voltages (instantaneous and rms), DC voltage and current, and real power are shown in Fig. 10. The parameters used for the simulation is shown in Table 2.

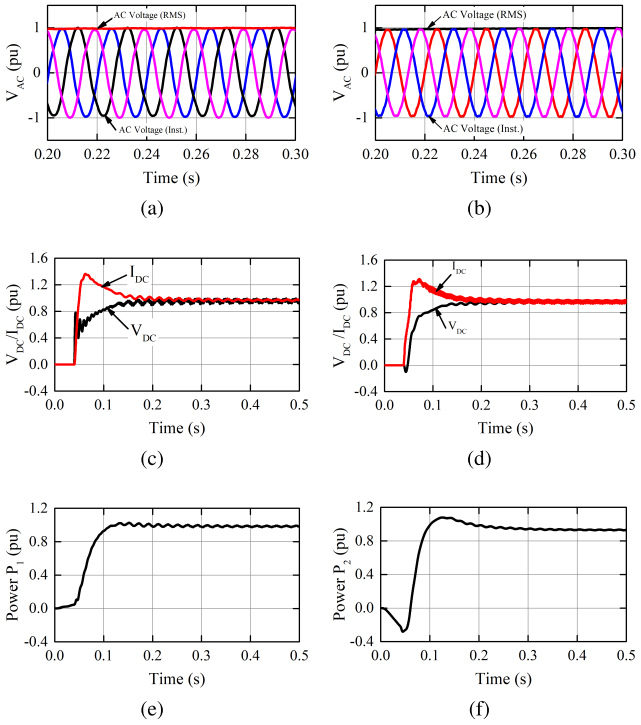

FIGURE 10. Simulation results of BTB LCC-HVDC system under steady-state condition. (a) V_{AC} on rectifier side. (b) V_{AC} on inverter side. (c) V_{DC} and I_{DC} on rectifier side. (d) V_{DC} and I_{DC} on inverter side. (e) P_1 on rectifier side. (f) P_2 on inverter side.

TABLE 2. Modified CIGRE HVDC benchmark system data used in simulation.

Parameters	Rectifier	Inverter
AC Voltage Base	230 kV	215 kV
Base MVA	100 MVA	100 MVA
Transf. tap (HV side)	1.01 pu	0.989 pu
Voltage Source	$1.088\angle 22.18^o$	$0.935\angle -23.14^o$
Nominal dc voltage	191.86 kV	191.86 kV
Nominal dc current	1 kA	1 kA
Transformer X_l	0.18 pu	0.18 pu
Source Impedance	R=3.737 Ω; $L = 0H$	R=0.7406 Ω ; $L = 0.0365H$
System Frequency	60 Hz	50 Hz
Minimum Angle	$\alpha = 15^o$	$\gamma = 15^o$

Fig. 10 shows the sending end AC voltage which is about 1.00 pu, DC voltage and current is about 0.998 pu, moreover, real power is about 0.998 pu. Similarly, at inverter side (receiving end) parameters are: AC voltage = 1.00 pu, DC voltage and current = 0.9790 pu and the real power = 0.9790 pu.

It is evident from the simulated results that overshoots appears in dc current during initial part of transient period and thereafter it attains steady-state condition.

B. DYNAMIC SIMULATIONS

The performance of BTB LCC-HVDC link under dynamic conditions is also evaluated using PSCAD/EMTDC based simulations. In this section, three types of faults are simulated, namely single-line-to-ground (LG) and double-line-to-ground (LLG) and line-to-line faults at inverter AC bus (receiving end side).

1) SINGLE-LINE-TO-GROUND FAULT

A single-line-to-ground fault is simulated at inverter AC bus (receiving end side) of the HVDC system. Fault starts at time $t = 0.30\ s$ and ends at $t = 0.35\ s$, hence, duration of fault is 0.05 s (2.5 cycles). Fig. 11 shows the simulation results of rectifier and inverter side AC voltages (instantaneous and rms), DC voltage and current, and real power under LG fault. It is evident from Fig. 11c that during the LG fault, DC current on rectifier side rises abruptly upto 2.5 times the steady-state value and settled at $t = 0.45\ s$ (settles within 0.15 s). Further, during the fault condition, DC voltage at rectifier side decreases sharply upto -0.5 pu from the normal value and settles down at $t = 0.45\ s$ (settles within 0.15 s). Also, the real power falls upto -0.15 pu on rectifier side and attains its steady-state (final) value at $t = 0.53\ s$ (Fig. 11e).

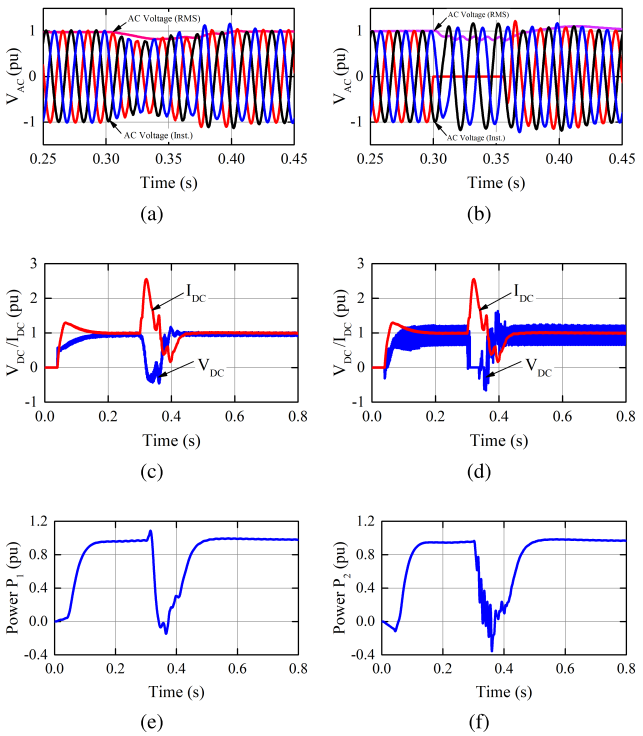

FIGURE 11. Simulation results of BTB LCC-HVDC system under LG fault at inverter AC bus. (a) V_{AC} on rectifier side. (b) V_{AC} on inverter side. (c) V_{DC} and I_{DC} on rectifier side. (d) V_{DC} and I_{DC} on inverter side. (e) P_1 on rectifier side. (f) P_2 on inverter side.

This shows the effect of LG fault on sending end while the fault appeared on the receiving end (at inverter AC bus).

Furthermore, from Fig. 11d, it is evident that during the LG fault condition, inverter side DC voltage dip is upto -0.63 pu and attains its final value at $t = 0.45s$. Also, during the LG fault, inverter side DC current rises suddenly upto 2.53 times the final value and settled at $t = 0.45$ s (settles within 0.15 s). The fault at inverter (AC side) results a dip in the AC voltage. Also, the commutating voltages are distorted in phase with reduced magnitude. This results in a corresponding decrease in the magnitude of DC voltage (V_{DC}) at the inverter side. This sudden drop in V_{DC} causes increase of the input DC current (I_{DC}) sharply to keep the real power (P) at the rated power level of the inverter station ($P = V_{DC}I_{DC}$).

The real power during the fault period on inverter side falls to approximately -0.4 pu and attains its final value at time, $t = 0.50$ s (i.e., it requires 0.20 s to resume its normal condition as shown in Fig. 11f).

2) DOUBLE-LINE-TO-GROUND (LLG) FAULT

A double-line-to-ground (LLG) fault at the inverter AC bus is simulated which starts at time $t = 0.30$ s and cleared at $t = 0.35$ s. Therefore, the fault duration is 0.05 s. The simulation results of rectifier side and inverter side AC voltages (instantaneous and rms), DC voltage and current, and real power under LLG fault condition are shown in Fig. 12. The rectifier side DC current rises suddenly upto 2.55 times the steady-state value during the LLG fault condition and settles after 0.15 s (Fig. 12c). At the same time, rectifier side DC voltage decreases sharply during the fault period upto -0.5 pu and settles down after 0.15 s. Moreover, the real power dips to -0.20 pu and attains its steady-state value at $t = 0.52$ s (Fig. 12e). Hence, the effect of fault appears on rectifier side (healthy side) while the LLG fault was occurred on the inverter side.

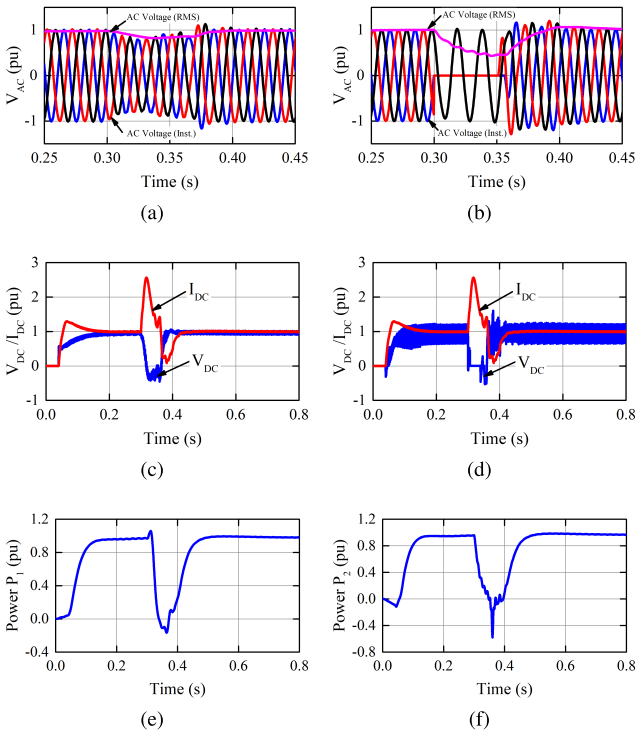

FIGURE 12. Simulation results of BTB LCC-HVDC system under LLG fault at inverter AC bus. (a) V_{AC} on rectifier side. (b) V_{AC} on inverter side. (c) V_{DC} and I_{DC} on rectifier side. (d) V_{DC} and I_{DC} on inverter side. (e) P_1 on rectifier side. (f) P_2 on inverter side.

During the LLG fault condition, the inverter side AC voltage dip is upto 0.4 pu from the normal value (Fig. 12b). The DC current on inverter side rises sharply upto 2.55 times the steady-state value during the LLG fault condition and settled after 0.15 s (Fig. 12d). At the same time, inverter side DC voltage decreases sharply upto -0.5 pu during the fault period and settles down after 0.15 s. Moreover, the real power dips to -0.60 pu and attains its final value at $t = 0.55$ s (Fig. 12f).

3) LINE-TO-LINE (LL) FAULT

A line-to-line (LL) fault at the inverter AC bus is simulated which starts at time $t = 0.30$ s and cleared at $t = 0.35$ s. Therefore, the fault duration is 0.05 s. The simulation results of rectifier side and inverter side AC voltages (instantaneous and rms), DC voltage and current, and real power under LL fault condition are shown in Fig. 13.

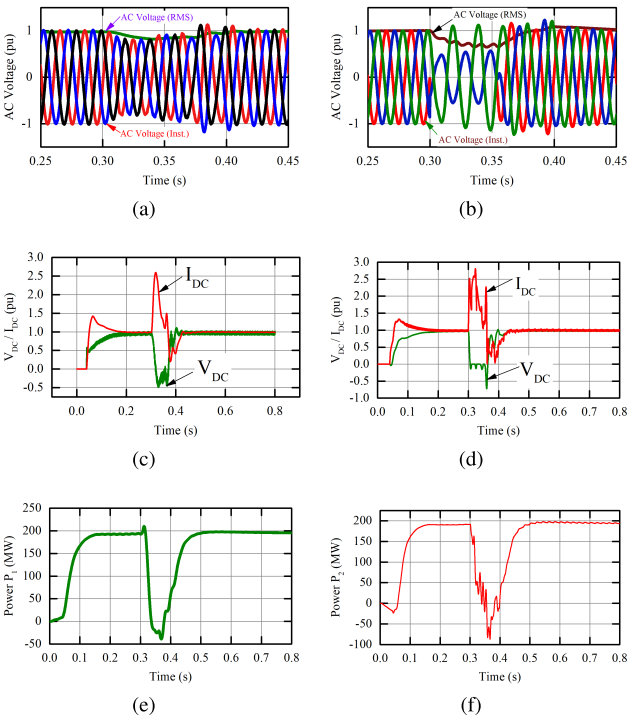

FIGURE 13. Simulation results of BTB LCC-HVDC system under LL fault at inverter AC bus. (a) V_{AC} on rectifier side. (b) V_{AC} on inverter side. (c) V_{DC} and I_{DC} on rectifier side. (d) V_{DC} and I_{DC} on inverter side. (e) P_1 on rectifier side. (f) P_2 on inverter side.

The rectifier side DC current rises suddenly upto 2.60 times the steady-state value during the LL fault condition and settles after 0.15 s (Fig. 13c). At the same time, rectifier side

TABLE 3. Comparative analysis of BTB LCC–HVDC link and FASAL system.

S.No.	BTB LCC–HVDC link	FASAL	Inference
1.	Under steady–state condition the reactive power demand is high and also requires large filter bank.	Under steady–state condition, reactive power demand is comparatively low and no need of filter bank.	Reactive power requirement is high in LCC-HVDC.
2.	It has low overload capability. If overloading is required, oversized capacity (oversized transformers, cooling system, cable, converters) becomes necessary [45].	It has substantial overload capacity because it is an electro-mechanical device to withstand the large transient current.	FASAL possesses high overload capacity as compared to a LCC-HVDC.
3.	During LG fault, the effect of fault is very significant on fault side as well as on healthy side. The rectifier DC current rises sharply to 2.55 times the normal value (Fig. 11c) and the real power dips to -0.40 pu on fault side. The effect of LG fault on healthy side grid is also significant as the active power dip was -0.15 pu (Figs. 11e and 11f).	During LG fault condition, the effect of fault is very small on stator current and voltage i.e., healthy side system (Fig. 6). Further, the active power dip is about 0.10 pu (20 MW) only on faulty side, whereas the effect of LG fault on healthy side grid is not significant as the active power dip was 0.06 pu (12 MW) only (Fig. 6e).	Effect of LG fault is high in BTB LCC-HVDC as compared to FASAL system.
4.	During LLG fault, the effect of fault is significant on both fault and healthy side. The rectifier DC current rises sharply to 2.55 times the normal value (Fig. 12c). Further, the real power dips to -0.60 pu on fault side and -0.20 pu on healthy side.	During LLG fault, the effect of fault is not significant on healthy side system, which is evident from Fig. 7. The active power dip is upto 0.125 pu (25 MW) only on fault side, whereas the active power dip was 0.075 pu (15 MW) only on healthy side as depicted in Fig. 7e.	Effect of LLG fault is significant on both sides in LCC-HVDC whereas the effect of fault is not significant on healthy side in FASAL.
5.	During LL fault, the DC current on rectifier side increases suddenly upto 2.75 times the rated value and settles down at $t = 0.13s$, as shown in Fig. 13c. Moreover, the real power on rectifier side dips to -0.25 pu and it attains its normal value at $t = 0.52s$ (Fig. 13e). The dip in AC voltage on inverter side is about 0.4 pu (Fig. 13b). There appears a transient DC voltage (dip of -0.75 pu) and a DC current (overshoots of 2.8 pu) during fault condition which settles down at $t = 0.43s$ (Fig. 13d). The active power also dips to about -0.75 pu (Fig. 13f).	During LL fault, the dip in active power is limited to 0.15 pu (30 MW) only which attains its final value within $0.7s$ (Fig. 8e). The Fig. 8e shows that the impact of fault on healthy side network is not significant as the oscillation and fluctuation in the active power were small (0.06 pu (12 MW) for $0.4s$ only). The dip in the rotor voltage is about 9 kV which attains its final value within $0.2s$ and there is very small impact on healthy side (stator side) as voltage fluctuation is about 1.5 kV only (Fig. 8g). There is very small impact on stator current due to fault on rotor side as depicted in Fig. 8c.	Impact of fault appears on rectifier side (healthy side) although the fault was applied on the inverter side in LCC-HVDC. No significant effect of healthy side FASAL.

DC voltage decreases sharply during the fault period upto -0.5 pu and settles down after 0.15 s. Moreover, the real power dips to -0.25 pu and attains its steady-state value at $t = 0.52$ s (Fig. 13e). Hence, the effect of fault appears on rectifier side (healthy side) while the LL fault was occurred on the inverter side.

During the LL fault condition, the inverter side AC voltage dip is upto 0.4 pu from the normal value (Fig. 13b). The DC current on inverter side rises sharply upto 2.8 times the steady-state value and contains fluctuations during the LL fault condition and settled after 0.15 s (Fig. 13d). At the same time, inverter side DC voltage decreases sharply upto -0.7 pu during the fault period and settles down after 0.15 s. Moreover, the real power dips to -0.45 pu as well as contains fluctuations and attains its final value at $t = 0.55$ s (Fig. 13f).

VII. COMPARISON OF FASAL SYSTEM WITH BTB LCC-HVDC SYSTEM

A comparative analysis between FASAL system and BTB LCC-HVDC system is made and described in the Table 3.

The comparison presented in Table 3 reveals that the FASAL system has many distinct advantages over BTB LCC–HVDC link in terms of (i) in-built natural damping ability due to the presence of large rotating inertia, and (ii) the effect of fault does not effect substantially the healthy side grid. Hence, the FASAL system is an alternative of BTB LCC-HVDC link with better steady-state and transient performance.

VIII. CONCLUSIONS

This paper has presented a comparative analysis of the performance of FASAL system and BTB LCC-HVDC system for electric power network interconnection. Some world-wide LCC-HVDC projects with their basic parameters are listed for quick review. The system description and steady-state mathematical model of proposed FASAL system and LCC-HVDC link are presented in this paper. The behaviour of FASAL system and BTB LCC-HVDC system during the steady-state as well as LG, LLG and LL fault conditions are evaluated using PSCAD/EMTDC based simulations.

It is observed that the FASAL system exhibits better performance than BTB LCC-HVDC system during the LG, LLG and the LL fault conditions. The behaviour of the FASAL system under fault condition is excellent as the healthy side remains almost unaffected while in BTB LCC-HVDC system the effect of fault is significantly high on the healthy side too. It is also evident from the results that the LCC-HVDC system consumed more reactive power than FASAL system.

APPENDIX A
PARAMETERS OF FASAL SYSTEM

PSN-I ratings: 230 kV, 240 MVA, 60 Hz;
Transformer-1 ratings: 230/20 kV, 240 MVA, 60 Hz;
Transformer-2 ratings: 230/20 kV, 240 MVA, 50 Hz;
PSN-II ratings: 230 kV, 240 MVA, 50 Hz.

APPENDIX B
DFIM SPECIFICATION AND PARAMETERS

$P_{rated} = 200$ MW, $V_1 = V_2 = 20$ kV, $f = 60$ Hz, $R_s = 0.0054$ pu, $R_r = 0.00607$ pu, $L_m = 4.362$ pu, $L_s = 0.102$ pu, $L_r = 0.110$ pu, H = 26 s.

REFERENCES

[1] P. Kundur, *Power System Stability and Control*. New York, NY, USA: McGraw-Hill, 1994.
[2] K. K. Sen and M. L. Sen, "Comparison of the 'Sen' transformer with the unified power flow controller," *IEEE Trans. Power Del.*, vol. 18, no. 4, pp. 1523–1533, Oct. 2003.
[3] K. Padiyar, *FACTS Controllers in Power Transmission and Distribution*. New Delhi, India: New Age International, 2007.
[4] N. G. Hingorani, L. Gyugyi, and M. El-Hawary, *Understanding FACTS: Concepts and Technology of Flexible AC Transmission Systems*. New York, NY, USA: IEEE Press, 2000.
[5] F. H. Gandoman, A. Ahmadi, A. M. Sharaf, P. Siano, J. Pou, B. Hredzak, and V. G. Agelidis, "Review of FACTS technologies and applications for power quality in smart grids with renewable energy systems," *Renew. Sustain. Energy Rev.*, vol. 82, pp. 502–514, Feb. 2018.
[6] R. Benabid, M. Boudour, and M. A. Abido, "Optimal location and setting of SVC and TCSC devices using non-dominated sorting particle swarm optimization," *Electr. Power Syst. Res.*, vol. 79, no. 12, pp. 1668–1677, Dec. 2009.
[7] R. Sirjani, A. Mohamed, and H. Shareef, "Optimal allocation of shunt var compensators in power systems using a novel global harmony search algorithm," *Int. J. Electr. Power Energy Syst.*, vol. 43, no. 1, pp. 562–572, Dec. 2012.
[8] D. Simon, "Biogeography-based optimization," *IEEE Trans. Evol. Comput.*, vol. 12, no. 6, pp. 702–713, Dec. 2008.
[9] H. Chen, A. R. Iyer, R. G. Harley, and D. Divan, "Dynamic grid power routing using controllable network transformers (CNTs) with decoupled closed-loop controller," *IEEE Trans. Ind. Appl.*, vol. 51, no. 3, pp. 2361–2372, May 2015.
[10] T. V. Charan and A. M. Parimi, "Comparision of interline power flow controller with line reactor and SSSC in a 400 kV transmission line," in *Proc. 3rd Int. Conf. Converg. Technol. (I2CT)*, Apr. 2018, pp. 1–6.
[11] K. Padiyar, *HVDC Power Transmission Systems: Technology and System Interactions*. New Delhi, India: New Age International, 1990.
[12] M. P. Bahrman and B. K. Johnson, "The ABCs of HVDC transmission technologies," *IEEE Power Energy Mag.*, vol. 5, no. 2, pp. 32–44, Mar./Apr. 2007.
[13] N. Flourentzou, V. G. Agelidis, and G. D. Demetriades, "VSC-based HVDC power transmission systems: An overview," *IEEE Trans. Power Electron.*, vol. 24, no. 3, pp. 592–602, Mar. 2009.
[14] L. Zhang, L. Harnefors, and H.-P. Nee, "Interconnection of two very weak AC systems by VSC-HVDC links using power-synchronization control," *IEEE Trans. Power Syst.*, vol. 26, no. 1, pp. 344–355, Feb. 2011.
[15] Y. Xue, X.-P. Zhang, and C. Yang, "Commutation failure elimination of LCC HVDC systems using thyristor-based controllable capacitors," *IEEE Trans. Power Del.*, vol. 33, no. 3, pp. 1448–1458, Jun. 2018.
[16] Y. Wang, W. Wen, C. Wang, H. Liu, X. Zhan, and X. Xiao, "Adaptive voltage droop method of multiterminal VSC-HVDC systems for DC voltage deviation and power sharing," *IEEE Trans. Power Del.*, vol. 34, no. 1, pp. 169–176, Feb. 2019.
[17] H. Wang and M. A. Redfern, "The advantages and disadvantages of using HVDC to interconnect AC networks," in *Proc. IEEE 45th Int. Universities Power Eng. Conf. (UPEC)*, Aug./Sep. 2010, pp. 1–5.
[18] K. K. Sen and M. L. Sen, "Introducing the family of 'SEN' transformers: A set of power flow controlling transformers," *IEEE Trans. Power Del.*, vol. 18, no. 1, pp. 149–157, Jul. 2003.
[19] K. K. Sen and M. L. Sen, "Unique capabilities of sen transformer: A power flow regulating transformer," in *Proc. IEEE Power Energy Soc. Gen. Meeting (PESGM)*, Jul. 2016, pp. 1–5.
[20] H. Fujita, S. Hara, K. J. Piwko, E. R. Pratico, and J. Sanchez-Gasca, "Simulator model of rotary power flow controller," in *Proc. Power Eng. Soc. Summer Meeting. Conf.*, vol. 3, Jul. 2001, pp. 1794–1797.
[21] A. O. Ba, T. Peng, and S. Lefebvre, "Rotary power-flow controller for dynamic performance evaluation—Part II: RPFC application in a transmission corridor," *IEEE Trans. Power Del.*, vol. 24, no. 3, pp. 1417–1425, Jul. 2009.
[22] D. Das, D. M. Divan, and R. G. Harley, "Power flow control in networks using controllable network transformers," *IEEE Trans. Power Electron.*, vol. 25, no. 7, pp. 1753–1760, Jul. 2010.
[23] P. Doyon, D. McLaren, M. White, Y. Li, P. Truman, E. Larsen, C. Wegner, E. Pratico, and R. Piwko, "Development of a 100 MW variable frequency transformer," presented at the Canada Power, Toronto, ON, Canada, Sep. 2004.
[24] A. Merkhouf, P. Doyon, and S. Upadhyay, "Variable frequency transformer—Concept and electromagnetic design evaluation," *IEEE Trans. Energy Convers.*, vol. 23, no. 4, pp. 989–996, Dec. 2008.
[25] P. E. Marken, J. J. Marczewski, R. D'Aquila, P. Hassink, J. H. Roedel, and R. L. Bodo, "VFT—A smart transmission technology that is compatible with the existing and future grid," in *Proc. IEEE/PES Power Syst. Conf. Exposit.*, Mar. 2009, pp. 1–7.
[26] B. Chen, W. Fei, C. Tian, L. Yang, and J. Gu, "A high-voltage sen transformer: Configuration, principles, and applications," *Energies*, vol. 11, no. 4, pp. 1–18, 2018.
[27] B. Chen, W. Fei, C. Tian, and J. Yuan, "Research on an improved hybrid unified power flow controller," *IEEE Trans. Ind. Appl.*, vol. 54, no. 6, pp. 5649–5660, Nov. 2018.
[28] A. O. Ba, T. Peng, and S. Lefebvre, "Rotary power-flow controller for dynamic performance evaluation—Part I: RPFC modeling," *IEEE Trans. Power Del.*, vol. 24, no. 3, pp. 1406–1416, Jul. 2009.

[29] Z. Chunpeng, J. Qirong, W. Yingdong, H. Chao, C. Yan, and S. Dan, "A series voltage compensator based on thyristor-controlled transformer," in *Proc. IEEE PES Asia–Pacific Power Energy Eng. Conf. (APPEEC)*, Nov. 2015, pp. 1–5.
[30] L. Contreras-Aguilar and N. García, "Stability analyses of a VFT park using a sequential continuation scheme and the limit cycle method," *IEEE Trans. Power Del.*, vol. 26, no. 3, pp. 1499–1507, Jul. 2011.
[31] P. Marken, J. Roedel, D. Nadeau, D. Wallace, and H. Mongeau, "VFT maintenance and operating performance," in *Proc. IEEE Power Energy Soc. Gen. Meeting - Convers. Del. Electr. Energy 21st Century*, Jul. 2008, pp. 1–5.
[32] D. Nadeau, "A 100-MW variable frequency transformer (VFT) on the hydro-Québec transénergie network—The behavior during disturbance," in *Proc. IEEE Power Eng. Soc. Gen. Meeting*, Jun. 2007, pp. 1–5.
[33] Imdadullah, S. M. Amrr, M. S. J. Asghar, I. Ashraf, and M. Meraj, "A comprehensive review of power flow controllers in interconnected power system networks," *IEEE Access*, vol. 8, pp. 18036–18063, 2020.
[34] Imdadullah, M. Irshad, M. S. J. Asghar, and S. J. Arif, "A flexible asynchronous AC link (FASAL) system," Indian Patent 296 524, May 4, 2018.
[35] S. Mirsaeidi, X. Dong, D. Tzelepis, D. M. Said, A. Dyśko, and C. Booth, "A predictive control strategy for mitigation of commutation failure in LCC-based HVDC systems," *IEEE Trans. Power Electron.*, vol. 34, no. 1, pp. 160–172, Jan. 2019.
[36] Imdadullah, M. Irshad, M. S. J. Asghar, and S. J. Arif, "Flexible asynchronous AC link for power system network interconnection," in *Proc. IEEE Energytech*, May 2012, pp. 1–6.
[37] Imdadullah, H. Rahman, and M. S. J. Asghar, "A flexible asynchronous AC link for two area power system networks," *IEEE Trans. Power Del.*, vol. 34, no. 5, pp. 2039–2049, Oct. 2019.
[38] L. Xu and Y. Wang, "Dynamic modeling and control of DFIG-based wind turbines under unbalanced network conditions," *IEEE Trans. Power Syst.*, vol. 22, no. 1, pp. 314–323, Feb. 2007.
[39] G. Abad, J. Lopez, M. Rodriguez, L. Marroyo, and G. Iwanski, *Doubly Fed Induction Machine: Modeling and Control For Wind Energy Generation*, vol. 85. Hoboken, NJ, USA: Wiley, 2011.
[40] E. G. Shehata, "Active and reactive power control of doubly fed induction generators for wind energy generation under unbalanced grid voltage conditions," *Electric Power Compon. Syst.*, vol. 41, no. 6, pp. 619–640, Apr. 2013.
[41] M. O. Faruque, Y. Zhang, and V. Dinavahi, "Detailed modeling of CIGRÉ HVDC benchmark system using PSCAD/EMTDC and PSB/SIMULINK," *IEEE Trans. Power Del.*, vol. 21, no. 1, pp. 378–387, Jan. 2006.
[42] M. E. Montilla-DJesus, D. Santos-Martin, S. Arnaltes, and E. D. Castronuovo, "Optimal operation of offshore wind farms with line-commutated HVDC link connection," *IEEE Trans. Energy Convers.*, vol. 25, no. 2, pp. 504–513, Jun. 2010.
[43] H. Ambriz-Pérez, E. Acha, and C. R. Fuerte-Esquivel, "High voltage direct current modelling in optimal power flows," *Int. J. Electr. Power Energy Syst.*, vol. 30, no. 3, pp. 157–168, Mar. 2008.
[44] D. Jovcic, *High Voltage Direct Current Transmission: Converters, Systems and DC Grids*. Hoboken, NJ, USA: Wiley, 2019.
[45] S. Henry, O. Despouys, R. Adapa, C. Barthold, K. Bell, J. Binard, A. Edris, P. Egrot, W. Hung, and G. Irwin, *Influence of Embedded HVDC Transmission on System Security and AC Network Performance*. Paris, France: Cigré, 2013.

IMDADULLAH (Member, IEEE) received the bachelor's degree in electrical engineering and the master's degree in power systems and drives from the Department of Electrical Engineering, Aligarh Muslim University (AMU), Aligarh, India, in 2003 and 2006, respectively, where he is currently pursuing the Ph.D. degree. Since December 2007, he has been working as an Assistant Professor of electrical engineering with University Polytechnic, AMU. He holds a patent on FASAL system and a concept of flexible asynchronous ac link. His research interests include renewable energy, power systems, instrumentation, and measurement.

ABDUL R. BEIG (Senior Member, IEEE) received the B.Eng. degree in electrical and electronics engineering from the National Institute of Technology Karnataka, Suratkal, India, and the M.Tech. and Ph.D. degrees in electrical engineering from the Indian Institute of Science, Bangalore, India. He is currently working as an Associate Professor with the Advanced Power and Energy Center, Department of Electrical Engineering and Computer Science, Khalifa University, Abu Dhabi, United Arab Emirates. His current research interests include auto tuning of grid connected converters, drive train in electric vehicles, multi-level converter, high-power drives, and SiC and GaN-based converters. He is also serving as an Associate Editor for the IEEE TRANSACTIONS ON INDUSTRIAL APPLICATIONS.

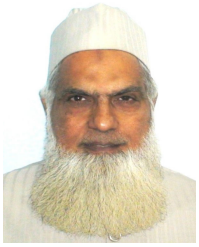

M. SYED JAMIL ASGHAR (Member, IEEE) was born in Patna, India. He received the B.Sc.Engg. degree in electrical, the M.Sc.Engg. degree in power systems, and the Ph.D. degree in power electronics from Aligarh Muslim University, Aligarh, India.

He joined the Department of Electrical Engineering, Aligarh Muslim University, in 1983, where he is currently a Professor. He has established the Centre of Renewable Energy, Department of Electrical Engineering, from the funds of UGC (Government of India). He is also a Coordinator of the DRS-II Program, UGC, Department of Electrical Engineering. He has written a text book, *Power Electronics* (Prentice-Hall of India). He is also a Chapter Author of *Power Electronics Handbook* (Academic/Elsevier, California, USA), under a Joint Program of the University of West Florida and the University of Florida, USA. He has successfully completed many Government Funded Research Projects and guided eight research (Ph.D.) theses. He holds five patents and many other patents are pending. He has published more than 60 papers in international journals and conference-proceedings, including several single-authored articles in the IEEE TRANSACTIONS. His research interests include power electronics, renewable energy systems, and electrical machines. He is a Fellow of IETE, India.